Analysis of the Ionization and Acceleration Efficiencies of Molecular Nitrogen in a Hall Effect Thruster

IEPC-2024-297

William P. Brabston[1], Luke A. Marino[2], Dan Lev[3], and Mitchell L. R. Walker[4]
Georgia Institute of Technology, Atlanta, GA, 30332, USA

   There is a growing interest in the efficient operation of Hall effect thrusters (HETs) on molecular propellants to expand the mission capabilities of HET-driven satellites. To inform on current inefficiencies seen in molecular-HET operation, an energy flow model is developed for HETs, utilizing a nitrogen propellant, that highlights the additional molecular energy paths and sinks compared to an atomic propellant. The distribution of input power among the energy pathways is driven by electron-impact kinetic mechanisms. New molecular-specific efficiency terms are developed to compare the relative efficiencies between each primary molecular ionization pathway. This model was then applied to experimental data on a 5-kW HET operating on nitrogen, argon, and xenon with a mass flow rate range of 5.0-5.4 mg/s and a discharge voltage range of 230-300 V. The measured thrust and anode thrust efficiency ranges on each propellant are 72.8-86.8 mN and 32.9-39.6% (xenon), 90.2-111.9 mN and 25.2-29.0% (argon), and 61.4-90.0 mN and 12.8-16.9% (nitrogen), respectively. The model shows that the low nitrogen thrust efficiency is primarily attributed to poor mass utilization of atomic nitrogen (~24%). Despite thrust efficiencies of less than 17% at these power levels, nitrogen exhibits promise operating above 5-kW due to the high voltage utilization seen with the N^+ species (~89%), likely caused by a temporally distinct N^+ ionization and acceleration region.

Nomenclature

A_{en}	=	Entrainment area, m^2
B	=	E×B applied magnetic field, G
d	=	E×B plate separation distance, m
e	=	Elementary charge, 1.602×10^{-19} C
E	=	Electric field strength, V/m
E/N	=	Reduced electric field, Td
$\mathcal{F}$	=	Faraday constant, 96,485 C/mol
$f(T_e)$	=	Electron velocity distribution function, m/s
I_{axial}	=	Axial component of beam current, A
I_b	=	Beam current, A
$I_{b,corr}$	=	Corrected beam current, A
$I_{b,n}$	=	Beam current of the nth species, A
I_d	=	Discharge current, A
$I_{d,corr}$	=	Corrected discharge current, A
k	=	Boltzmann constant, 1.38×10^{-23} m^2kg/s^2K

---

[1] Graduate Student, School of Aerospace Engineering, wbrabston3@gatech.edu

[2] Graduate Student, School of Aerospace Engineering, lukemarino54@gatech.edu

[3] Research Engineer, School of Aerospace Engineering, dan.lev@gatech.edu

[4] Professor and School Chair, School of Aerospace Engineering, mitchell.walker@ae.gatech.edu

k_j	=	Reaction rate of the jth mechanism, m^3/s
$\dot{m}_a$	=	Anode mass flow rate, mg/s
$\dot{m}_{en}$	=	Entrained background neutral mass flow rate, mg/s
$\dot{m}_i$	=	Ion mass flow rate, mg/s
$\dot{m}_{i,n}$	=	Ionic mass flow rate of nth species, mg/s
$\mathcal{M}_n$	=	Molar mass of nth species, g/mol
m_n	=	Mass of nth particle, kg
$\dot{m}_n$	=	Mass flow rate of nth species, mg/s
N	=	Neutral number density, m^{-3}
P	=	Chamber background pressure, Torr or Pa
P_d	=	Discharge power, W
Q	=	Average charge state of ionic particles
T	=	Thrust, mN
T_{corr}	=	Corrected thrust, mN
T_e	=	Electron temperature, eV
T_0	=	Neutral temperature, K
V_a	=	Atomic averaged acceleration voltage, V
$V_{a,n}$	=	Average acceleration voltage of the nth species, V
V_d	=	Discharge voltage, V
V_p	=	Plasma potential, V
$\bar{v}$	=	Average particle velocity, m/s
$\overline{v^2}$	=	Averaged particle squared velocity, m^2/s^2
y_0	=	Normalized neutral particle speed
Z_j	=	Charge state of the jth charge species
$\Delta V_{plate,n}$	=	E×B plate voltage at n^{th} species peak
ζ_A	=	Area entrainment factor
ζ_{en}	=	Thrust entrainment factor
η_b	=	Current utilization
η_E	=	Energy efficiency
η_{SP}	=	Species parameter efficiency
η_T	=	Anode thrust efficiency
η_V	=	Voltage utilization
$\eta_{V,n}$	=	Species voltage utilization of nth species
θ_d	=	Beam divergence angle, deg
ξ_n	=	Species fraction
ξ_N	=	Species fraction of atomic nitrogen
σ_{d,N_2}	=	Electron-impact diatomic nitrogen dissociation cross section, m^2
$\sigma_{i,N}$	=	Electron-impact atomic nitrogen ionization cross section, m^2
σ_{i,N_2}	=	Electron-impact diatomic nitrogen ionization cross section, m^2
σ_j	=	Electron-impact cross section for the jth mechanism, m^2
Φ_m	=	Mass utilization
$\Phi_{m,n}$	=	Species mass utilization
Φ_{N-G}	=	Neutral-gain utilization
Φ_P	=	Propellant efficiency
Φ_q	=	Charge utilization
Ψ_b	=	Beam efficiency
$\Omega_{i,n}$	=	Current fraction of nth species
Ω_j	=	Current fraction of the jth charge species
$\langle \rangle_m$	=	Mass averaged quantity
$\langle \rangle_{mv}$	=	Momentum averaged quantity

I. Introduction

A current high-interest area in the field of electron propulsion (EP) is enabling satellites to access very low Earth orbit (VLEO), which is generally defined as orbits less than 450 km. VLEO offers numerous benefits due to its close positioning to Earth, including better latency on communication systems along with higher resolution imaging of Earth and numerous other benefits[1,2]. While VLEO is an attractive orbit for satellites, it is currently prohibitive in that the drag satellites experience is much higher than in further orbits. This is demanding on the satellite propulsive systems to generate enough thrust to compensate for the additional drag, greatly expands the propellant budget, and greatly limits mission life for satellites using traditional xenon or krypton propellant[1,3].

One such solution to the propellant budget issue is employing on-orbit in-situ propellant harvesting of nitrogen and oxygen to decrease the size of propellant tanks and potentially allow satellites to remain in VLEO orbits indefinitely. However, atmospheric propellants are molecular in nature, and when used in a Hall effect thruster (HET), present unique challenges with their ability to dissociate. Dissociation leads to additional energy sinks and ionization mechanisms that are not present with atomic propellants. These additional mechanisms seen with molecular propellants severely degrade the performance of molecular propellant HETs, often to a point where the thrust cannot overcome the atmospheric drag[4-7]. Pure nitrogen[8,9] and air mixtures[10-12] tested in HETs have both exhibited highly degraded performance and efficiency compared to more traditional atomic propellants.

Munro O'Brien *et al.* tested a low-power HET (30-810 W), with xenon, krypton, argon, and nitrogen. They found that nitrogen exhibited the lowest thrust and anode thrust efficiency at 5.7 mN and 5.4%, respectively, compared to 12.6 mN and 26.3% for xenon, 6.9 mN and 15.2% for krypton, and 6.6 mN and 9.6% for argon[8]. Ferrato *et al*. operated a $0.56N_2 + 0.44O_2$ air mixture in a mid-power HET (1.2-5.2 kW). They measured thrust and anode thrust efficiency values from 30 mN to 120 mN and 8% to 18%, respectively[10]. The efficiency values greatly underperform typical mid-power HET anode thrust efficiencies operating on xenon or krypton, which are generally over 50%[13,14]. Both of these tests recognize poor mass utilization of the molecular propellants as a primary contributor to the low resultant anode efficiency.

To understand where HET inefficiencies originate and influence more optimized HET design, Hofer presented a phenomenological efficiency model[15,16], which Brown expanded into an analytical efficiency model for atomic propellants in a HET[17,18]. These models decompose thrust efficiency into a series of efficiency terms that are independently empirically measured from diagnostics in the HET plume and, when multiplied together, result in the overall measured thrust efficiency. This efficiency architecture quantifies the effect of various energy sinks present within a HET that result in a decrease in thrust efficiency.

While this existing atomic efficiency architecture fits well with experimental data and offers insights into sources of efficiency degradation, it is limited in that is based on assumptions that are only valid for atomic propellants in a HET. Some of the base assumptions of these models are that all ionic species have the same mass and acceleration voltage, which begin to break down when applied to molecular propellants. Furthermore, molecular propellants can dissociate and become rotationally and vibrationally excited[4], which can both lead to a degraded efficiency and are not captured in the atomic efficiency architectures.

The goal of this paper is to analyze the dominant kinetic mechanisms that drive the ionization of a diatomic nitrogen propellant in a HET and evaluate the impact of these mechanisms on thrust efficiency. These mechanisms will be viewed through the lens of energy conservation in an energy flow model and applied to an updated molecular efficiency model influenced by Hofer and Brown's approach. These models are then applied to experimental data on a 5-kW HET to better understand how the kinetic mechanisms vary with a changing discharge voltage and the resultant effect on thrust efficiency.

II. Efficiency and Energy Flow Model of a Hall Thruster

The following subsections introduce efficiency and energy flow models for atomic and molecular propellants in a HET. The first subsection summarizes the standard atomic efficiency model developed by Hofer[15] and Brown[17]. To visualize the efficiency model components and ionization processes using an energy approach, an energy flow model for the ionization and acceleration of an atomic propellant is then introduced. The second subsection expands this energy flow model to account for the additional energy pathways seen with molecular propellants in a HET. The next subsection introduces additional molecular efficiency terms that account for the additional energy pathways seen with molecular propellants. Finally, the last subsection discusses the most probable kinetic reactions seen with nitrogen ionization in a HET along with their respective cross-sections.

A. Atomic Efficiency Model and Energy Flow Diagram

The existing atomic efficiency architecture analytically decomposes anode thrust efficiency (η_T), as defined in Eq. (1), into energy (η_E), propellant (Φ_P), and beam efficiencies (Ψ_b) as outlined in Brown[17].

$$\eta_T = \frac{\frac{1}{2}T^2}{\dot{m}_a P_d} = \left\{ \frac{\frac{1}{2}\dot{m}_a \langle \overline{v^2} \rangle_m}{P_d} \right\} \left\{ \frac{\langle \bar{v} \rangle_m^2}{\langle \overline{v^2} \rangle_m} \right\} \left\{ \langle cos\theta_d \rangle_{mv}^{\;2} \right\} = \eta_E \Phi_P \Psi_b \tag{1}$$

This equation starts with η_T in its standard definition using thrust (T), mass flow rate to the anode ($\dot{m}_a$), and discharge power (P_d), where T is further expanded into a function of the averaged particle velocity (v) components and beam divergence (θ_d). In Eq. (1), $\langle\;\rangle_m$ represents a mass averaged quantity and $\langle\;\rangle_{mv}$ signifies a momentum averaged quantity. Analytical expressions for η_E, Φ_P, and Ψ_b are derived by grouping the components of η_T as seen in Eq. (1).

η_E represents how effectively a thruster converts input power into jet power and can be expanded into a product of current utilization (η_b) and voltage utilization (η_V) as outlined in Eq. (2), with the assumption that all charge species are subject to the same acceleration voltage (V_a). At unity energy efficiency, current utilization and voltage utilization are also both unity. Unity current utilization is achieved when all cathode electrons neutralize the beam and no electrons make it to the anode, causing beam current (I_b) to equal discharge current (I_d). Unity voltage utilization is achieved when V_a is equivalent to the input discharge voltage (V_d), causing ions to be subject to the full acceleration potential.

$$\eta_E = \left\{ \frac{V_a}{V_d} \right\} \left\{ \frac{I_b}{I_d} \right\} = \eta_V \eta_b \tag{2}$$

Φ_P represents how effectively a thruster utilizes the propellant mass. At peak efficiency, a thruster ionizes the entire propellant mass to a single charge state, and deviations from this ideal state will result in a loss of propellant efficiency. Φ_P can be expanded into a charge utilization (Φ_q), mass utilization (Φ_m), and neutral-gain utilization (Φ_{N-G}) as seen in Eq. (3), with the assumption that all charge species have the same mass. In this equation, Ω_j is the current fraction of the jth charge species, Z_j is the charge state of the jth charge species, $\dot{m}_i$ is the mass flow rate of the plume ions, y_0 is the average neutral speed normalized by the average ion speed, and Q is the average ion charge state.

$$\Phi_P = \left\{ \frac{\left[\sum_{j=1} \left(\frac{\Omega_j}{\sqrt{Z_j}} \right) \right]^2}{\sum_{j=1} \left(\frac{\Omega_j}{Z_j} \right)} \right\} \left\{ \frac{\dot{m}_i}{\dot{m}_a} \right\} \left\{ 1 + 2y_o \frac{1-\Phi_m}{\Phi_m \sqrt{Q\Phi_q}} \right\} = \Phi_q \Phi_m \Phi_{N-G} \tag{3}$$

Ψ_b captures the drop in overall efficiency due to the off-axis component of jet momentum, where at maximum efficiency the velocity vector of all accelerated ions will be aligned with the axial thrust vector. Ψ_b can generally be approximated using the measured axial beam current (I_{axial}) as shown in Eq. (4), assuming the charge species current fraction is constant across all plume angles.

$$\Psi_b = \langle cos\theta_d \rangle_{mv}^{\;2} \approx \left(\frac{I_{axial}}{I_b} \right)^2 \tag{4}$$

For a maximum anode thrust efficiency, all input power besides that used in ionization is transferred to jet power parallel to the thrust vector, and all input propellant mass is ionized to a +1 charge state. However, in reality, this is never possible since thrusters contain energy sinks that prevent all input power from converting into jet power. The breakdown of thrust efficiency into an analytical efficiency architecture grants insight into which energy sinks in a HET have the largest impact on decreasing thrust efficiency. With conservation of energy principles, input power can be tracked through a HET using an energy flow model as a graphical tool to more easily visualize where some of the energy sinks originate while the efficiency architecture predicts the relative impact of each energy sink. A representative energy flow diagram for an atomic propellant in a HET is shown in Fig. 1, where the corresponding efficiency term that relates to each energy sink is indicated.
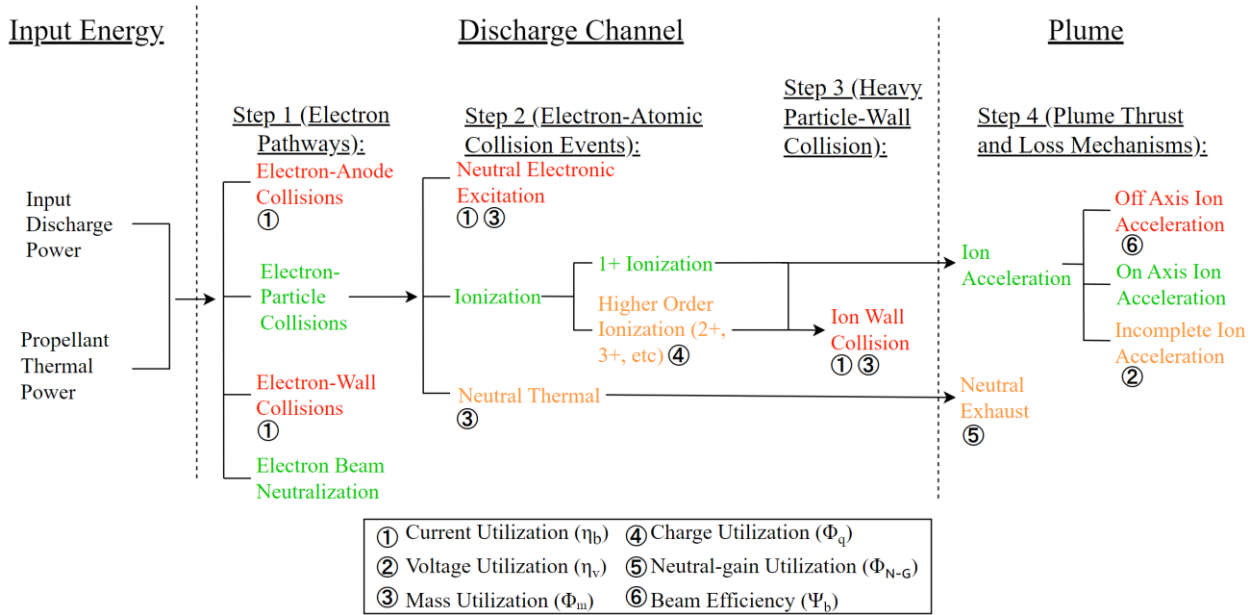
4

Figure 1. Energy flow diagram of an atomic propellant in a HET. Green represents the maximum efficiency path, orange represents an inefficient energy path that will still produce some thrust, and red represents an energy sink that will not produce thrust.

The energy flow diagram is organized by the path through which input energy moves through a HET. The discharge power first transfers to electrons as they accelerate toward the discharge channel, where this power is either lost to the thruster body via electron-thruster collisions or transferred to neutral particles via electron-neutral collisions. After an electron collision, the neutral particles either ionize with sufficient energy and accelerate or excite one of their energy modes[13]. If all input energy travels along the green pathway in the energy flow diagram, the thruster would operate at maximum thrust efficiency and any energy that travels down an orange or red path causes a reduction in thrust efficiency.

The efficiency architecture provides a holistic view of these energy sinks and predicts the relative impact of all the energy sinks that contribute to each efficiency term, as shown in the energy flow diagram. For greater fidelity to each of these energy sinks, additional studies directly measure some of these energy terms[19-21].

B. Diatomic Energy Flow Diagram

In modifying the energy flow model to apply to molecular propellants, it is important to recognize the additional energy sinks and pathways that arise through the molecular ionization process. This can be seen through the addition of energy paths to account for the dissociation and excitation of the rotational and vibrational energy modes. The updated molecular energy flow diagram is shown in Fig. 2. This energy flow diagram is shown for a diatomic molecule that can only ionize to a +1 charge state, but could be further expanded for other non-diatomic molecules and additional charge states.
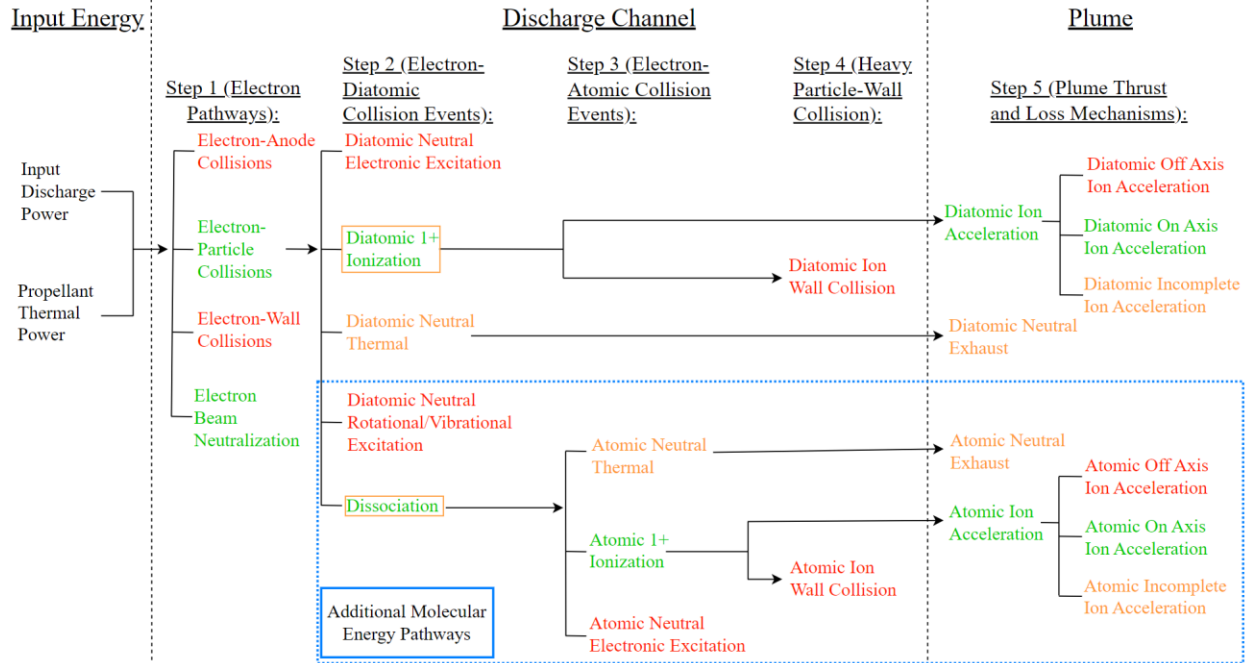
5

Figure 2. Energy flow diagram of a diatomic propellant in a HET. Green represents the maximum efficiency path, orange represents an inefficient energy path that will still produce some thrust, and red represents an energy sink that will not produce thrust.

Two immediate conclusions from the diatomic energy flow diagram are that the dissociation process greatly expands the number of potential energy pathways possible with molecular propellants, as seen with the additional molecular energy pathways box, and that there are two pathways that are designated as efficient pathways. The dissociation process splits the diatomic energy flow diagram into an atomic and diatomic pathway, which are visually similar in the diagram, but as will be seen later in this paper, differ in experimentally measured values. Atomic ions, such as N^+, can be produced from molecules via a two-step dissociation and ionization collisional process, whereas molecular ions, such as N_2^+, are generally produced in a one-step direct ionization process[10,22-24]. The time delay from the two-step collisional process to produce atomic ions may cause the atomic and molecular ions to experience distinct ionization and acceleration regions that vary temporally.

The energy that travels down the atomic compared to the molecular pathway will experience different energy sinks and impact thrust efficiency to a different extent. To produce an efficient molecular HET, it is important to recognize which pathway is most efficient for a given thruster at a given setpoint. For these reasons, it is not immediately certain whether it is more efficient to produce atomic or molecular ions at a given thruster operating condition, which is why dissociation and the diatomic 1+ ionization paths are both green and orange in the above figure.

C. Molecular Efficiency Terms

Since molecular propellants produce multiple potentially efficient ionization and acceleration pathways, the need arises to compare the efficiencies between the various pathways. To do this, new pertinent molecular efficiency terms are derived, based on the framework of the atomic efficiency architecture presented in Section II.A. The first pertinent molecular efficiency term is species fraction $\left(\xi_n = \frac{\dot{m}_n}{\dot{m}_a}\right)$, where $\dot{m}_n$ is the mass flow rate of the nth species, both neutral and ionic states. ξ_n indicates the extent of dissociation, and can inform on the power split between both ionization pathways. The next pertinent efficiency terms are species mass utilization $\left(\Phi_{m,n} = \frac{\dot{m}_{i,n}}{\dot{m}_n}\right)$ and species voltage utilization $\left(\eta_{V,n} = \frac{V_{a,n}}{V_d}\right)$, where $\dot{m}_{i,n}$ is the mass flow rate of the nth ionic species and $V_{a,n}$ is the acceleration voltage applied to the nth ionic species. $\Phi_{m,n}$ and $\eta_{V,n}$ can be different for each ionic species produced from a molecular propellant (e.g. N^+ and N_2^+), which captures their potentially distinct ionization and acceleration processes.

To compare the relative efficiencies between the production of different ionic species in a molecular propellant, another new efficiency term is defined and denoted as species parameter efficiency (η_{SP}) as shown in Eq. (5). η_{SP} is

a useful metric in that it contains the largest contributing path dependent efficiency terms, and is thus a singular value that can be used to compare relative pathway efficiencies. For example, with a nitrogen propellant, η_{SP} will indicate the relative efficiencies in producing N^+ versus N_2^+ species, which could experience different ionization and acceleration regions. If the N species η_{SP} is greater than the N_2 species η_{SP}, this indicates that it is more efficient to produce a N^+ ionic species over N_2^+, and thus a dissociative ionization process that creates N^+ would be preferential over a direct-ionization process that creates N_2^+.

$$\eta_{SP} = \eta_{V,n}\Phi_{m,n} \tag{5}$$

D. Nitrogen Ionization Kinetic Mechanisms

The distribution in input power among the molecular energy pathways is driven by nitrogen electron-impact kinetic mechanisms in the HET discharge channel. An electron collision with a neutral, diatomic nitrogen molecule can either result in an ionization or dissociation event, excite the electronic, rotational, or vibrational internal energy modes, add thermal energy to the molecule, or be any combination of these events. The probability of each of these events occurring can vary as the plasma parameters change, such as local electron temperature (T_e), plasma density, neutral density, and reduced electric field (E/N). For E/N, E is the strength of the local electric field and N is the neutral number density, where E/N is generally described in units of Townsend (Td).

HETs have a high E/N (~1×10^6 Td) due to the generation of strong local electric fields from electron confinement[13]. For a nitrogen plasma with a high E/N (over 1×10^3 Td), the total input power transferred to the vibrational, rotational, and electronic internal energy modes becomes negligible compared to the power applied to the dissociation and ionization processes[25,26]. Therefore, at high E/N, the dominant kinetic mechanisms in a nitrogen plasma become direct ionization and dissociation mechanisms, which are summarized in Table 1. This table also provides the electron-impact cross-section for the jth mechanism (σ_j) at a 30 eV electron temperature and associated reaction energy. The cross-sections for each of these mechanisms across a range of electron temperatures are shown in Fig. 3.

Table 1. Probable nitrogen kinetic mechanisms.

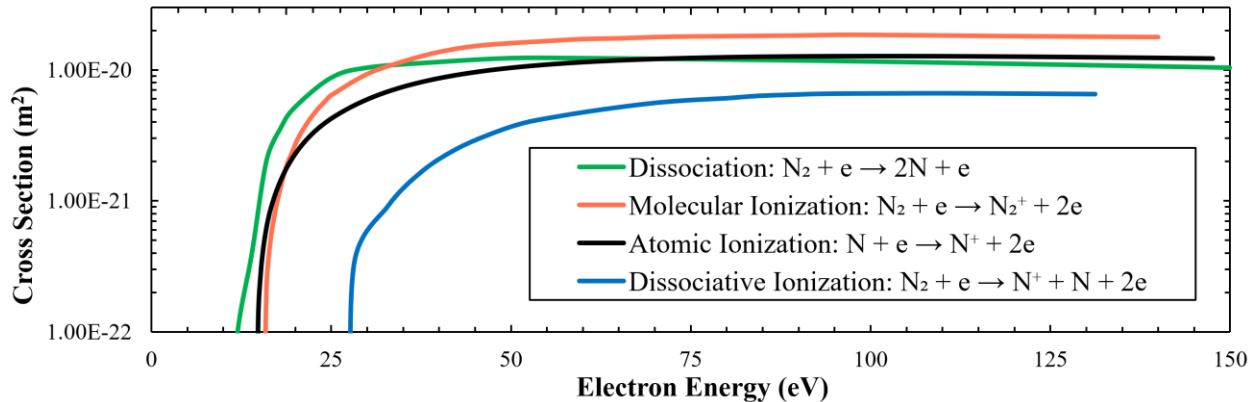| Reaction	Reaction Type	$\sigma_j(T_e = 30\text{ eV}), (m^2)$	Reaction Energy, (eV)	Ref
$N_2 + e \rightarrow 2N + e$	Dissociation	1.04×10^{-20}	9.76	(Ref. 23)
$N_2 + e \rightarrow N_2^+ + 2e$	Molecular ionization	9.29×10^{-21}	15.58	(Ref. 22)
$N + e \rightarrow N^+ + 2e$	Atomic ionization	5.94×10^{-21}	14.53	(Ref. 24)
$N_2 + e \rightarrow N^+ + N + 2e$	Dissociative ionization	3.25×10^{-22}	26.67	(Ref. 22)

Figure 3. Nitrogen electron-impact cross sections[22-24].

As seen in the above table and plot, dissociation of nitrogen is the dominant mechanism at low electron temperatures (~10-25 eV) whereas direct molecular ionization becomes the dominant mechanism at higher electron temperatures (>35 eV). While ionization of a neutral N_2 particle into N^+ can occur in a singular electron collision

7

event, this mechanism is much less likely than first dissociating N_2 into N and then ionizing N into N^+ via a separate electron collision. Using the provided cross-sections, the reaction rate of the j$^{\text{th}}$ mechanism (k_j) is calculated using Eq. (6), where $f(T_e)$ is the electron velocity distribution function[27].

$$k_j = \sigma_j \times f(T_e) \tag{6}$$

III. Experimental Design and Test Setup

The following subsections overview the test design and diagnostics used to collect the data for use in the energy and efficiency models. This includes the thruster setpoints chosen, characteristics of the chamber and thruster used, and test configuration of each of the diagnostics. This section concludes with a discussion of probe corrections to account for background pressure and an approximation for the species fraction term.

A. Test Overview

The authors performed an experimental test using nitrogen in a HET to determine how thruster parameters affect the distribution of power across the atomic and molecular energy pathways and how this distribution affects thrust efficiency. This test features nitrogen as a propellant due to its prevalence in air breathing electric propulsion and inert nature, and argon and xenon serve as comparative atomic propellants. Argon is the atomic propellant most similar to nitrogen in terms of mass, ionization energy, and ionization cross section[28], and will provide the most direct comparison of nitrogen's distinct molecular contributions on efficiency. Xenon is historically a commonly used atomic propellant and for this reason will also provide a good comparison for nitrogen. Table 2 presents an outline of the mass and ionization energy of all species present in this experiment.

Table 2. Propellant species properties.

Species	Mass, (amu) (Ref. 29)	First Ionization Energy, (eV) (Ref. 29)
Xe	131.29	12.13
Ar	39.95	15.76
N_2	28.02	15.58
N	14.01	14.53

For each setpoint, mass flow rate and discharge voltage are matched between the propellants. The range of mass flow rates and discharge voltages tested are based on the stable operating regions of the HET operating on nitrogen, as nitrogen has the narrowest stability region. For each propellant, the magnetic field is adjusted to minimize discharge current and discharge current peak-to-peak oscillations, then kept constant for the remainder of the setpoints. The chosen setpoints (N3, Ar3, and Xe3) to optimize the magnetic field are selected since they share the most common operational parameters to the rest of the setpoints. The setpoint operating parameters for nitrogen, argon, and xenon are outlined in Table 3, Table 4, and Table 5, respectively. All setpoints use xenon as the cathode gas which is maintained at 4.5 sccm. In the following tables, the peak radial magnetic field is measured in the center of the discharge channel at the thruster exit plane.

Table 3. HET operational setpoints on nitrogen

Setpoint	Anode Flow Rate [N_2], mg/s (sccm)	Cathode Flow Rate [Xe], mg/s (sccm)	Discharge Voltage, (V)	Discharge Power, (kW)	Peak Radial B-field, (G)	Chamber Pressure, (Torr, N_2)
N1	5.0 (240)	0.44 (4.5)	231.9	3.08	130	1.47×10^{-5}
N2	5.0 (240)	0.44 (4.5)	255.1	3.69	130	1.14×10^{-5}
N3	5.0 (240)	0.44 (4.5)	278.6	4.30	130	1.19×10^{-5}
N4	5.2 (250)	0.44 (4.5)	277.0	4.56	130	1.38×10^{-5}
N5	5.4 (260)	0.44 (4.5)	275.7	4.81	130	2.14×10^{-5}

8

Table 4. HET operational setpoints on argon.

Setpoint	Anode Flow Rate [Ar], mg/s (sccm)	Cathode Flow Rate [Xe], mg/s (sccm)	Discharge Voltage, (V)	Discharge Power, (kW)	Peak Radial B-field, (G)	Chamber Pressure, (Torr, Ar)
Ar1	5.0 (168.3)	0.44 (4.5)	229.1	3.34	130	2.41×10^{-5}
Ar2	5.0 (168.3)	0.44 (4.5)	253.7	3.75	130	2.55×10^{-5}
Ar3	5.0 (168.3)	0.44 (4.5)	278.9	4.13	130	1.22×10^{-5}
Ar4	5.2 (175.3)	0.44 (4.5)	277.5	4.36	130	2.98×10^{-5}
Ar5	5.4 (182.4)	0.44 (4.5)	276.1	4.58	130	4.15×10^{-5}
Ar6	5.0 (168.3)	0.44 (4.5)	303.6	4.68	130	2.39×10^{-5}

Table 5. HET operational setpoints on xenon.

Setpoint	Anode Flow Rate [Xe], mg/s (sccm)	Cathode Flow Rate [Xe], mg/s (sccm)	Discharge Voltage, (V)	Discharge Power, (kW)	Peak Radial B-field, (G)	Chamber Pressure, (Torr, Xe)
Xe1	5 (50.9)	0.44 (4.5)	230.8	1.75	162.5	4.49×10^{-5}
Xe2	5 (50.9)	0.44 (4.5)	250.3	2.15	162.5	3.94×10^{-5}
Xe3	5 (50.9)	0.44 (4.5)	274.3	2.03	162.5	3.28×10^{-5}

B. Vacuum Test Facility and Thruster

All measurements for the investigation are performed in Vacuum Test Facility 1 (VTF-1) at the High-Power Electric Propulsion Lab (HPEPL) at Georgia Tech. VTF-1 measures 7 m in length by 4 m in diameter and reaches high vacuum using a set of six 48" diffusion pumps. With the diffusion pumps, VTF-1 achieves a base pressure of 1 $\times$ 10^{-6} Torr, operational pressures between 1.1×10^{-5} and 4.5×10^{-5} Torr corrected for the respective gas, and a maximum calculated effective pumping speed of 292,000 l/s of N_2. Pressure measurements were taken using an SRS IGC100 ion gauge controller and Kurt J. Lesker G100F ion gauge located coincident to the exit plane of the thruster, and the calculation for effective pumping speed was based on the best practice pressure guidelines[30]. Tables 3-5 present the operational pressure for each setpoint and Fig. 4 illustrates the layout of the chamber along with probe positioning for this test.
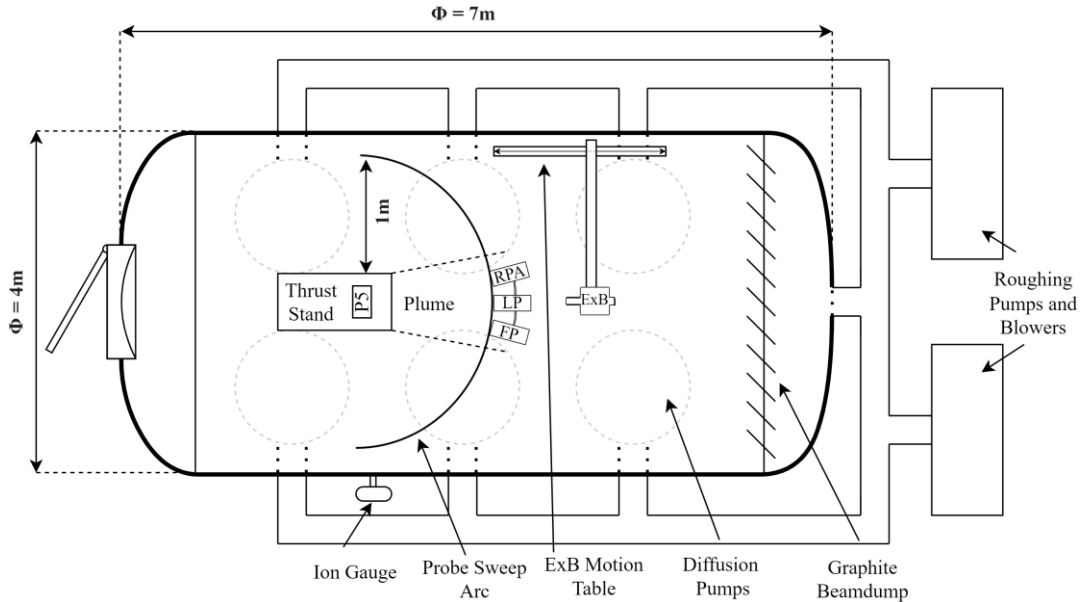

Figure 4. Schematic of VTF-1.

The thruster used for all setpoints in this test campaign is the P5 5-kW HET. Gulczinski[31] presents the engineering drawings of the P5, which is described in detail and is configured as outlined in Haas[32]. The P5 uses an EPL HCPEE 500 externally mounted cathode for all setpoints, positioned at the 12 o'clock position with the orifice located 2.2 cm downstream of the thruster exit plane and 14.7 cm above the thruster centerline. A Regatron TC.P.10.1000.480.S.HMI TopCon Quadro power supply provides the discharge power and TDK-Lambda power supplies power the magnets (type GEN 40-38), cathode heater (type GEN 20-76), and keeper (type GEN 150-10). The P5 operates with a discharge filter installed, with a resistance value of 1.4 Ω in series and capacitance of 79.7 μF in parallel to the discharge circuit.

The authors selected the P5 HET for this test due to its designed robustness as a laboratory thruster, relatively long 32 mm discharge channel length compared to most other mid-power thrusters, which effectively increases the residence time of the lightweight nitrogen particles in the discharge channel, and the myriad of comparative historical performance data. Historically, the P5 has operated primarily on xenon propellant at mass flow rates from 5.25 mg/s to 15 mg/s and discharge voltages of 200-600 V with presented performances of 65-400 mN of thrust, 1000-2700 s of specific impulse, and anode thrust efficiencies of 34-56%[16,31-33]. Some of this historical data is presented later, alongside the data from this experiment, in the results sections of this paper. Note that the xenon setpoints in this test have a mass flow rate of 5 mg/s, which is off-nominal from what has been run historically, but was chosen to match the mass flow rate of the stable setpoints of nitrogen. The thruster body was electrically floated for all setpoints.

MKS GE50A mass flow controllers (MFCs) meter the anode and cathode and their operational flow rates are calibrated with a MesaLabs DryCal 800. The MFCs have an uncertainty of 1% of the current setpoint leading to a maximum test uncertainty of ± 0.05 mg/s.

C. Diagnostics

Thrust is measured using a null-type inverted pendulum thrust stand fitted with a TE Connectivity HR 100 linear varying differential transformer (LVDT). The thrust stand is configured and operated as detailed in the recommended practices for thrust measurements[34]. An installed calibration string calibrates the thrust stand signal and is set to a range of 0 – 194.7 mN for this test, which was set based on the predicted thrust response of all propellants. This thrust measurement setup results in a maximum test uncertainty of ± 2.6 mN for nitrogen, ± 4.3 mN for argon, and ± 4.9 mN for xenon.

An E×B probe, or Wien filter, measures the charge and mass species current fractions along with the species acceleration voltage for nitrogen. This probe is mounted on a two-axis Parker Daedal 803-9922A linear motion table, configured as outlined in Kim and Gallimore[35] and Gurciullo et al.[36], and positioned 1 m downstream of the thruster exit plane on the thruster centerline for all measurements. The current fraction of the nth species $(\Omega_{i,n})$ is calculated using a bi-Gaussian fit of the current trace as recommended in the literature[36,37]. $V_{a,n}$ for each species is calculated according to Eq. (7) as a function of plate voltage at the nth species peak $(\Delta V_{plate,n})$, plate separation distance (d), particle mass of the nth species (m_n), the elementary charge of a +1 ion (e), and applied E×B magnetic field (B)[36], corrected by local plasma potential (V_p). A sample nitrogen E×B trace with the bi-Gaussian fit is shown in Fig. 5.

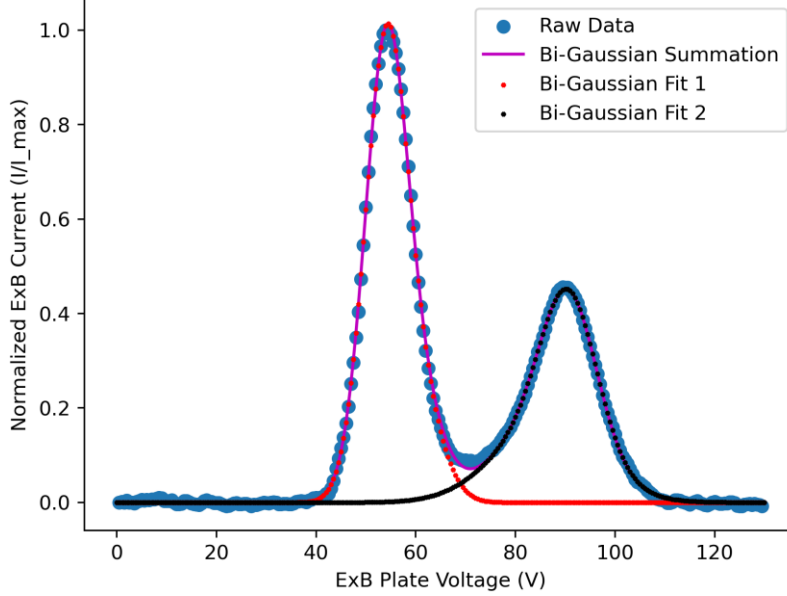$$V_{a,n} = \frac{e}{2} m_n \left(\frac{\Delta V_{plate,n}}{dB}\right)^2 - V_p \tag{7}$$

Figure 5. Sample nitrogen ExB trace with bi-Gaussian fit.

A Langmuir probe, Faraday probe, and retarding potential analyzer (RPA) are installed on a theta probe arm that sweeps from -90° to +90° at 1 m downstream of the thruster exit plane as shown in Fig. 4. The Langmuir probe is a cylindrical type, constructed with a 0.11-mm diameter tungsten filament with a length of 14.8 mm where voltage is supplied and current is measured using a Keithley 2470 Sourcemeter. For this dataset, the Langmuir probe measures V_p with the processes outlined in Lobbia[38].

The Faraday probe is a JPL nude type with a 22 mm diameter tungsten-coated aluminum collector separated with a 1.15 mm gap from an aluminum guard ring, as presented in Frieman *et al.*[39] and Walker *et al.*[40]. This is swept from -90° to 90°, at an angular spacing of 0.2°, in a 1 m radius arc with a collector potential of -50 V with respect to ground, where the voltage is supplied and current is measured using a Keithley 2470 Sourcemeter. Beam current and beam divergence are post-processed from the Faraday measurements using the procedures and equations laid out in the Faraday probe recommended practices paper[41]. Due to asymmetries in the plume, the beam current is calculated using measurements from -90° to 0° and 0° to +90°, then averaged for the resultant total beam current. I_b from the Faraday probe and $\Omega_{i,n}$ from the E×B probe are used to calculate $\dot{m}_{i,n}$ according to Eq. (8), where $\mathcal{M}_n$ is the molar mass of the nth species and $\mathcal{F}$ is Faraday's constant.

$$\dot{m}_{i,n} = \frac{\Omega_{i,n} I_b \mathcal{M}_n}{\mathcal{F}} \tag{8}$$

The RPA configuration consists of a five-grid layout, with a floating grid, two electron suppression grids biased at -50 V with respect to ground, an ion repulsion grid that sweeps from 0 to $(V_d + 50)$ V, and copper collector grid as detailed in Xu[42]. A Keithley 2470 Sourcemeter supplies the voltage to the ion repulsion grids in increments of 1 V, a Xantrex XPD 60-9 power supply holds the -50 V potential on the electron repulsion grids, and a Keithley 6485 Picoammeter measures the current from the collector. The RPA measures V_a, corrected by V_p, for xenon and argon.

D. Background Pressure Correction

Background neutrals can cause T, I_d, and I_b to be artificially higher than in ideal vacuum conditions[43,44]. Typically, these parameters are corrected for elevated pressures by varying chamber pressure to find the approximately linear relationship between these parameters and chamber pressure. This relationship is then extrapolated to a perfect vacuum condition[18,41]. Since VTF-1 has a relatively high operational pressure, this method was not feasible for this test. The data was instead corrected by using a neutral ingestion model that was proposed by Randolph[45], and modified by Reid[46] and Brown[18]. Brown demonstrated the approach to be accurate when compared to the more commonly used method of varying chamber pressure[18]. In this model, the entrained background neutral mass flow rate ($\dot{m}_{en}$) into the

11

discharge channel is approximated using the kinetic particle flux equation across a hemisphere centered at the thruster exit plane and reduced into Eq. (9).

$$\dot{m}_{en} = A_{en}P\sqrt{\frac{m_n}{2\pi kT_0}} \tag{9}$$

A_{en} is the area of the hemisphere, calculated as 488 cm^2 for the P5, P is the background chamber pressure in Pa, k is Boltzmann's constant, and T_0 is the temperature of the background neutrals, which is assumed to be 300 K. The entrained flow is then assumed to be ionized and accelerated into the beam, which causes the artificial increase in I_d, I_b, and T. The actual entrained mass flow can vary from what is presented in Eq. (9) and entrained mass that is ionized generally does not contribute as much to thrust as mass that originates from the anode, so an area entrainment factor (ζ_A) and thrust entrainment factor (ζ_{en}) are introduced as corrections to match empirical data trends. The equations for corrected I_d, I_b, and T are shown in Eq. (10-12), respectively[18].

$$I_{d,corr} = I_d - \zeta_A \dot{m}_{en} \frac{e}{m_n} \tag{10}$$

$$I_{b,corr} = I_b + \zeta_A \dot{m}_{en} \frac{e}{m_n} \tag{11}$$

$$T_{corr} = T\left(1 - \zeta_{en}\frac{\dot{m}_{en}}{\dot{m}_a + \dot{m}_{en}}\right) \tag{12}$$

The correction factors are set to $\zeta_A = 1.0$ as was done in Reid[46] and $\zeta_{en} = 0.8$, which was scaled by power and mass flow trends seen in Brown[18] for the conditions in this test. Error propagation for all diagnostics was performed by using standard methods outlined in NIST Technical Note 1297[47], with maximum calculated uncertainties for each measured parameter presented in Table 6.

Table 6. Maximum diagnostic uncertainty using standard error propagation.

Propellant	T	Ω_{in}	V_p	I_b	$V_{a,n}$ (E×B)	V_a (RPA)
Nitrogen	±2.6 mN	±0.05	±0.25 V	±0.34 A	±11.6 V	~
Argon	±4.3 mN	±0.07	±0.25 V	±0.48 A	~	±4.4 V
Xenon	±4.9 mN	±0.10	±0.25 V	±0.46 A	~	±4.5 V

E. Species Fraction Approximation

With the current set of plasma diagnostics used for this experiment, ξ_n cannot be directly measured since biased plasma probes cannot detect the neutral particles that contribute to ξ_n. The value for ξ_N, being species fraction for atomic nitrogen, for this test is approximated using Eq. (13), where $\dot{m}_N/\dot{m}_{i,N_2}$ is assumed to be a function of the nitrogen dissociation $\left(\sigma_{d,N_2}\right)$ and ionization $\left(\sigma_{i,N_2}\right)$ cross sections at a given T_e.

$$\xi_N = \frac{\dot{m}_N}{\dot{m}_a} = \left\{\frac{\dot{m}_N}{\dot{m}_{i,N_2}}\right\}\left\{\frac{\dot{m}_{i,N_2}}{\dot{m}_a}\right\} \approx \left\{\frac{\sigma_{d,N_2}(T_e)}{\sigma_{i,N_2}(T_e)}\right\}\left\{\frac{\dot{m}_{i,N_2}}{\dot{m}_a}\right\} = \left\{\frac{\sigma_{d,N_2}(T_e)}{\sigma_{i,N_2}(T_e)}\right\}\left\{\frac{\Omega_{i,N_2}I_b}{\dot{m}_a}\frac{\mathcal{M}_{N_2}}{\mathcal{F}}\right\} \tag{13}$$

In this approximation, T_e in the discharge channel is assumed to scale with V_d as presented in Raitses et al.[13,48]. This corresponds to a T_e range of 29.5 eV to 38.4 eV for the tested nitrogen V_d range, which relates to a σ_{d,N_2} range of 9.82×10^{-21} to 1.14×10^{-20} m^2 and a σ_{i,N_2} range of 8.81×10^{-21} to 1.31×10^{-20} (Ref. 22, 23). For future experiments, ξ_N can be more accurately measured using optical emission spectroscopy (OES) with a collisional radiative model or two-photon absorption laser induced florescence (TALIF) at the thruster exit plane, where both techniques have been performed for flowing nitrogen plasmas[49-52].

IV. Results and Discussion

The following subsections present the probe results and discussions from the aforementioned setpoints. The first subsection focuses on overall performance and efficiency trends across all setpoints. The subsequent subsections then discuss the rationale for the dominant kinetic mechanisms seen in the nitrogen ionization process and how these

12

mechanisms influence the resultant thrust efficiency. Fig. 6 shows operational pictures of the P5 firing on each propellant.
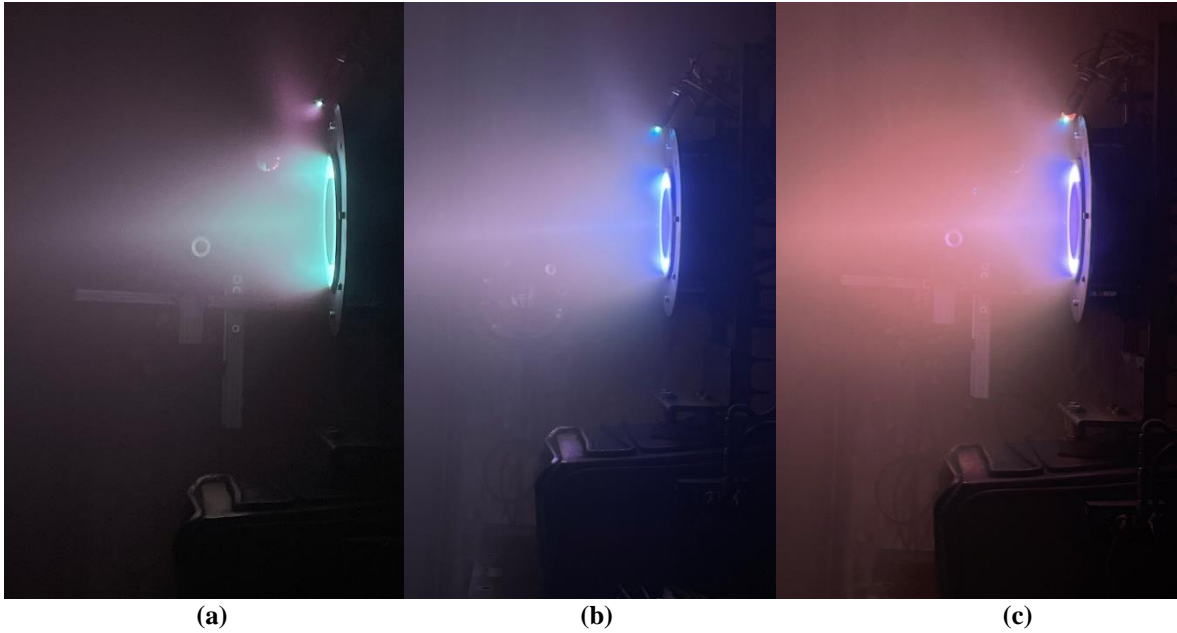

<div align="center">(a)   (b)   (c)</div>

Figure 6. P5 operating on (a) xenon, (b) argon, and (c) nitrogen propellant.

A. Overall Performance and Efficiency Trends

Thrust and anode thrust efficiency, as calculated from thrust measurements, are presented for all setpoints and propellants in Fig. 7 and 8, respectively. Historical xenon data from Hofer[16], Gulczinski[31], and Walker[33] are superimposed on each plot to verify the xenon setpoints still match historical trends, even though they are taken at an off-nominal low mass flow rate. Since the mass flow rate was matched between each of the propellants, the P5 operated at a much lower power for xenon in this test compared to argon and nitrogen due to xenon's large particle mass. The historical xenon data scales beyond the power range of xenon for this test and also allows for comparisons to the argon and nitrogen data at similar power levels.
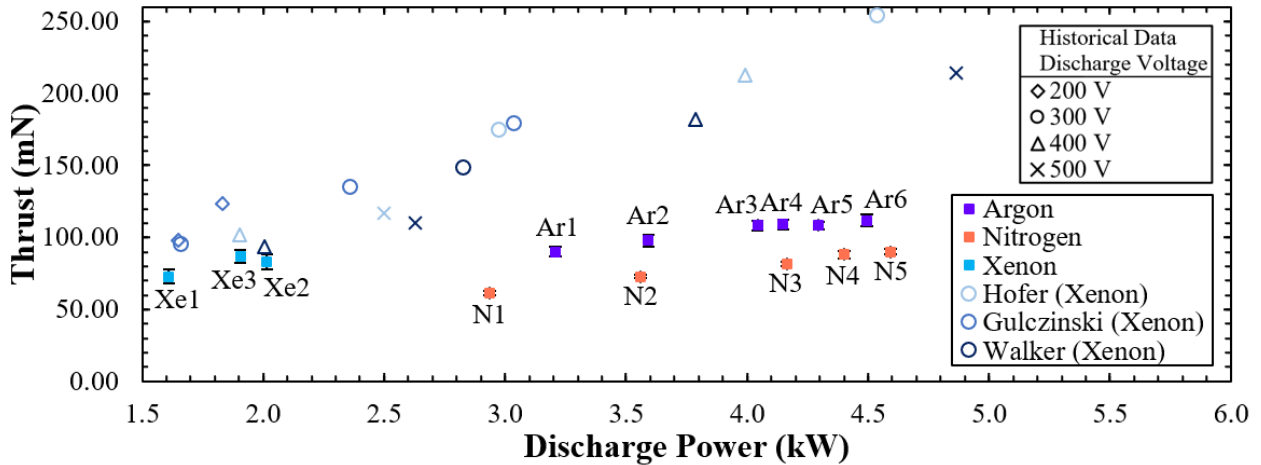

Figure 7. P5 HET thrust as a function of discharge power on xenon, argon, and nitrogen. VTF-1 data had a $\dot{m}_a$ range of 5.0-5.4 mg/s and V_d range of 229-304 V. Historical data has a $\dot{m}_a$ and V_d range of 5.3-14.6 mg/s and 300-500 V (Hofer)[16], 5.7-10.3 mg/s and 200-300 V (Gulczinski)[31], and 5.3-10.5 mg/s and 300-500 V (Walker)[33], respectively. All historical data was run on xenon.
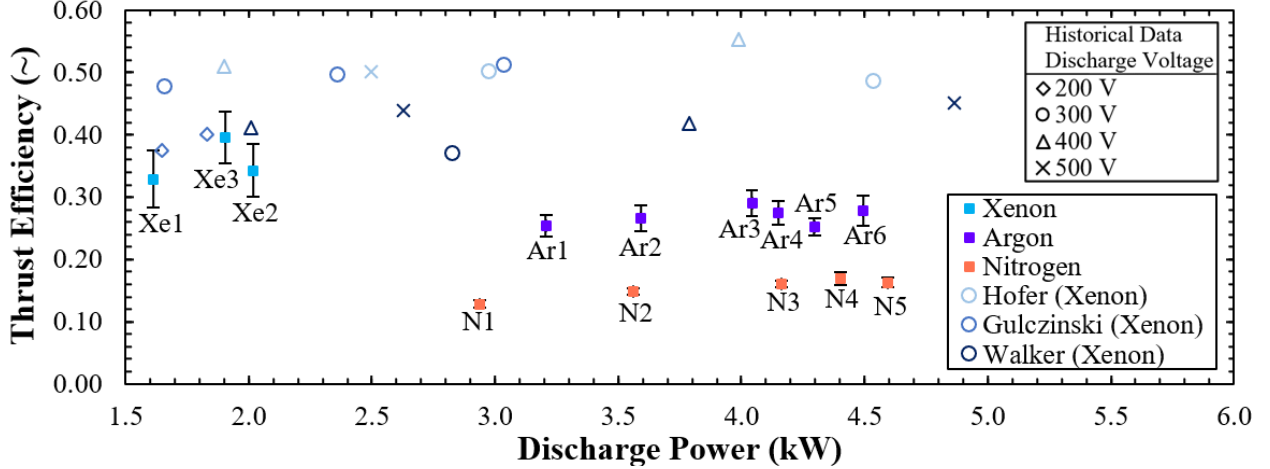
Figure 8. P5 HET thrust efficiency as a function of discharge power on xenon, argon, and nitrogen. VTF-1 data had a $\dot{m}_a$ range of 5.0-5.4 mg/s and V_d range of 229-304 V. Historical data has a $\dot{m}_a$ and V_d range of 5.3-14.6 mg/s and 300-500 V (Hofer)[16], 5.7-10.3 mg/s and 200-300 V (Gulczinski)[31], and 5.3-10.5 mg/s and 300-500 V (Walker)[33], respectively. All historical data was run on xenon.

As seen in the above figures, the xenon points measured in VTF-1 match relatively close to the trends found in the P5 historical data despite operating at a mass flow rate that is out-of-family from what has been tested historically. At similar powers, nitrogen is seen to exhibit a lower thrust and anode thrust efficiency than argon and xenon, similar to what is seen in existing literature[8,9]. Despite their similar mass and ionization energies, nitrogen notably showed a much lower η_T ($\approx$ 30-50%) across all setpoints compared to argon. This is likely due to the molecular nature of nitrogen, which will be further analyzed in the following subsections.

B. Species Production Rates and Dissociation Region

To understand how to optimize a nitrogen HET, a good understanding of the dominant kinetic processes in a HET discharge channel and how these processes scale with thruster operating conditions is needed. Since many kinetic processes are highly dependent on E/N and T_e as discussed in Section II.D., and V_d has a strong correlation to these parameters[13], species production is tracked as a function of V_d with all other thruster parameters held constant. Species production is measured with the nth species contribution to beam current $\left(I_{b,n}\right)$ and species fraction of atomic nitrogen $\left(\xi_N = \frac{\dot{m}_N}{\dot{m}_a}\right)$. ξ_N tracks the total dissociation ratio and $I_{b,n}$ tracks individual ionic species production. These parameters are presented in Table 7 and the trends are plotted in Fig. 9.

Table 7. Nitrogen species currents and species fraction. $\dot{m}_a$ = 5 mg/s for all setpoints.

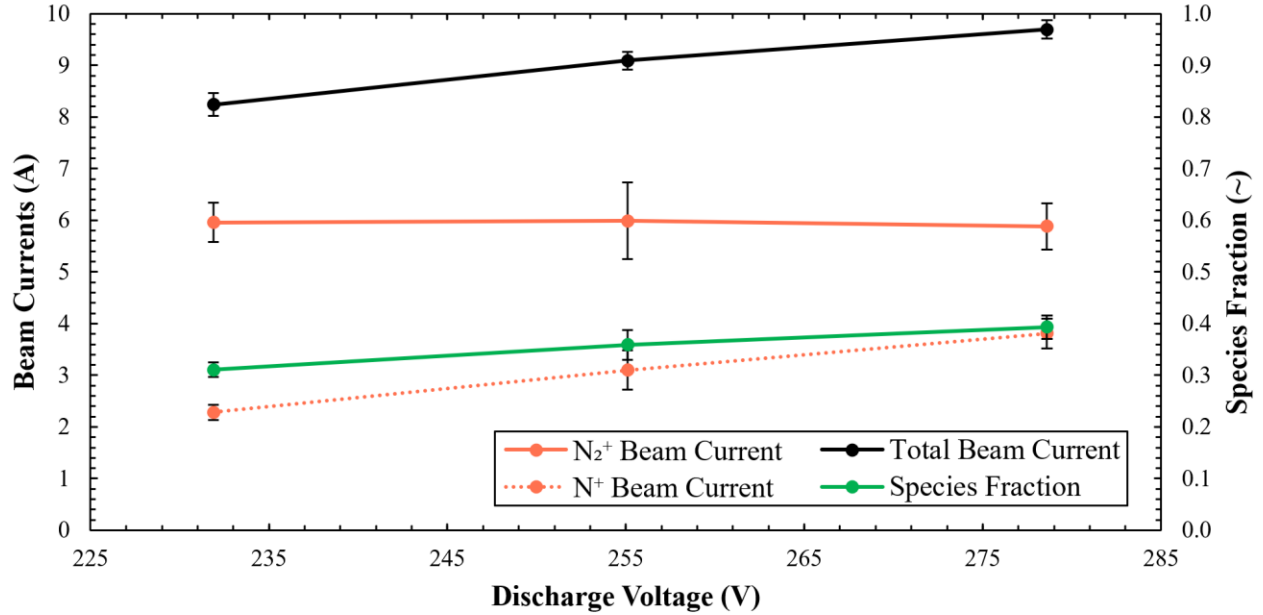| Setpoint	V_d, (V)	I_d, (A)	I_b, (A)	I_{b,N_2}, (A)	$I_{b,N}$, (A)	ξ_N
N1	231.9	12.7	8.24 ± 0.22	5.96 ± 0.38	2.28 ± 0.14	0.31 ± 0.01
N2	255.1	14.0	9.09 ± 0.17	5.99 ± 0.74	3.10 ± 0.38	0.36 ± 0.03
N3	278.6	14.9	9.69 ± 0.18	5.88 ± 0.45	3.81 ± 0.29	0.39 ± 0.02

14

Figure 9. P5 beam current and species fraction trends on nitrogen propellant as a function of discharge voltage. $\dot{m}_a = 5$ **mg/s for all setpoints.**

From the trends in Fig. 9, it is seen that I_b, ξ_N, and $I_{b.N}$ clearly increase monotonically as a function of V_d, while I_{b,N_2} stays approximately constant. This is a surprising result because it is seen in Fig. 3 that for $T_e \approx 30$ eV, σ_{i,N_2} has the largest slope compared to σ_{d,N_2} and the atomic nitrogen ionization cross-section $(\sigma_{i,N})$. As seen in Eq. (6), the reaction rate of a given mechanism is a direct function of its associated cross-section. If ionization and dissociation of nitrogen occur in the same region in the discharge channel at the same time, the relative production rates of N^+ and N_2^+ and the dissociation rate, represented by ξ_N, should scale as a function of their respective cross-sections as V_d and T_e change. The fact that I_{b,N_2} remains relatively constant over the measured V_d range while $I_{b,N}$ and ξ_N definitively increase must imply that dissociation and ionization cannot entirely occupy the same region in the discharge channel. Thus, there must be a region in the discharge channel where dissociation is dominant and ionization is unlikely, and this region, denoted as the dissociation region, likely extends closer to the anode than the primary ionization region. A schematic of the predicted distributions of the dissociation, ionization, and acceleration regions is presented in Fig. 10.
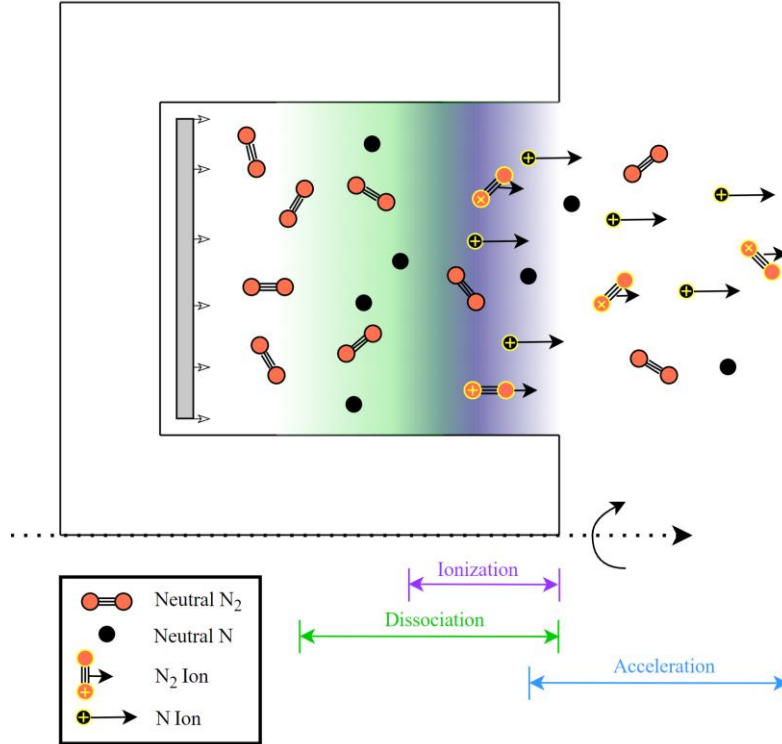
15

Figure 10. Kinetic mechanism model of the predicted regions where dissociation, ionization, and acceleration occur spatially in the discharge channel of a nitrogen-operated HET. Shown is a cross-section of a HET discharge channel, where the grey rectangle represents the anode. Figure is not drawn to scale.

Internal measurements in the P5 discharge channel indicate that upstream of the ionization region, T_e will drop at spatial distances closer to the anode[53]. Since the dissociation energy of nitrogen is lower than its ionization energy as seen in Table 1, and for a low T_e, σ_{d,N_2} becomes much greater than σ_{i,N_2} as seen in Fig. 3, it is reasonable to assume that the dissociation mechanism can dominate closer to the anode. Since this is the first region where the neutral nitrogen molecules enter after leaving the anode, the strength of this dissociation region controls the ratio of neutral species that enter the ionization region. For a dissociation region that induces high reaction rates of dissociation, which may occur at a higher V_d, there will be fewer available neutral N_2 molecules to ionize in the ionization region and more available N to ionize. Even though in the ionization region the reaction rate of the molecular ionization mechanism is greater than the reaction rate of the atomic ionization mechanism, having less available N_2 to ionize and more available N to ionize could result in I_{b,N_2} remaining relatively constant and $I_{b,N}$ strongly increasing as V_d increases.

Based on the presented kinetic mechanism model within a HET discharge channel, the dissociation mechanism will dominate in the dissociation region upstream of the primary ionization region. The dissociation region will control the dissociation rate with a molecular HET, which determines the relative power split between the atomic and molecular energy flow pathways represented in Fig. 2. As particles enter the primary ionization region, dissociation collisions still occur, but the molecular and atomic ionization mechanisms also become dominant mechanisms and this is where the majority of ionization occurs. Atomic ionization via a singular dissociative-ionization collision can also occur in the primary ionization region; however, the low relative cross-section of this mechanism makes it much less likely than a two-collision dissociation and ionization process. Acceleration of all ionic species will then occur close to the exit plane of the HET.

C. Molecular Efficiencies and Time-Varying Species Concentrations

In developing an efficient molecular HET, it is also important to understand how the various kinetic mechanisms within the discharge channel impact thrust efficiency. To do this, the relative energy sinks along the atomic and molecular nitrogen pathways are tracked using the $\Phi_{m,n}$, $\eta_{V,n}$, and η_{SP} molecular efficiency terms developed in Section II.C. These terms are then compared with the similar Φ_m and η_V terms from the atomic efficiency model applied to the argon and xenon setpoints. Once again, the setpoints selected in this analysis are those that vary V_d

16

while keeping all other thruster operating parameters constant. These efficiency terms are presented in Table 8 for nitrogen, argon, and xenon and the trends as a function of V_d are plotted in Fig. 11.

Table 8. Species efficiencies of nitrogen with comparison to argon and xenon. $\dot{m}_a = 5$ mg/s for all setpoints.

Setpoint	V_d, (V)	I_d, (A)	Φ_m	η_V	η_{SP}
			Nitrogen		
N1	231.9	12.7	N: 0.21 ± 0.01	N: 0.91 ± 0.05	N: 0.19 ± 0.01
			N_2: 0.50 ± 0.04	N_2: 0.72 ± 0.05	N_2: 0.36 ± 0.04
N2	255.1	14.0	N: 0.25 ± 0.02	N: 0.90 ± 0.04	N: 0.22 ± 0.02
			N_2: 0.54 ± 0.08	N_2: 0.68 ± 0.04	N_2: 0.37 ± 0.06
N3	278.6	14.9	N: 0.28 ± 0.03	N: 0.88 ± 0.04	N: 0.25 ± 0.03
			N_2: 0.56 ± 0.04	N_2: 0.64 ± 0.04	N_2: 0.36 ± 0.03
			Argon		
Ar1	229.1	14.0	0.78 ± 0.03	0.77 ± 0.02	~
Ar2	253.7	14.2	0.76 ± 0.04	0.77 ± 0.01	~
Ar3	278.9	14.5	0.79 ± 0.06	0.80 ± 0.02	~
			Xenon		
Xe1	230.8	7.0	0.90 ± 0.07	0.74 ± 0.02	~
Xe2	250.3	8.1	0.87 ± 0.06	0.75 ± 0.02	~
Xe3	274.3	6.9	0.87 ± 0.05	0.79 ± 0.02	~

Intuitively, one would think that producing more N_2^+ would be much more efficient than producing more N^+ from nitrogen, since N_2^+ avoids the energy cost of dissociation, is a larger particle with a higher ionization cross-section, and can ionize via a one-step direct ionization process as opposed to the two-step ionization process seen with N^+. For the voltage range from 230-275 V, Fig. 11 agrees with this intuition as it shows that η_{SP}, which is a measure of relative species efficiency, for N_2^+ is higher than for N^+. This indicates that across these setpoints, N_2^+ is, in fact, more efficient to produce than N^+. Therefore, energy that travels down the atomic ionization pathway experiences stronger energy sinks and degrades the overall thrust efficiency to a greater extent than energy that travels down the molecular ionization pathway. However, the gap between the η_{SP} values begins to converge from a 17% difference to an 11% difference across this V_d range. η_{SP} for N_2^+ is seen to remain relatively constant while η_{SP} for N^+ monotonically increases, which accounts for the convergence between the species.

From the $\Phi_{m,n}$ term, it is seen that Φ_{m,N_2} is much higher than $\Phi_{m,N}$ across all V_d, while both are lower than Φ_m for both xenon and argon. Φ_{m,N_2} is approximately where the predicted value would lie just due to differences in ionization cross section and mass between argon and nitrogen. $\Phi_{m,N}$, on the other hand, is much lower and decreases the total mass utilization and thrust efficiency for nitrogen. This indicates that many of the N particles do not have enough time to both dissociate and ionize before leaving a region in the discharge channel with sufficiently high electron temperature; however, the trends suggest that increasing V_d greatly mitigates this
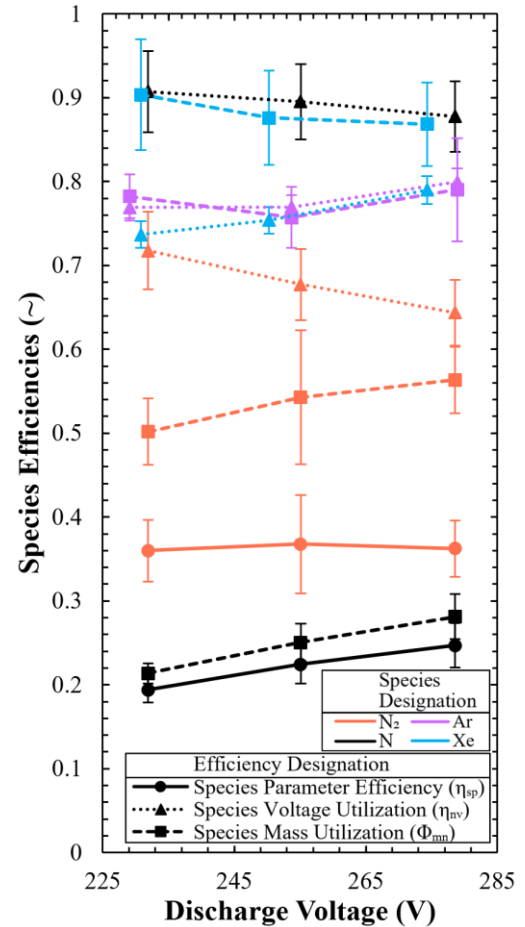

Figure 11. Species efficiencies for nitrogen from molecular efficiency model as a function of discharge voltage. Similar xenon and argon efficiencies from atomic efficiency model are superimposed for comparison. $\dot{m}_a = 5$ mg/s for all setpoints.

17

effect. As V_d increases, $\Phi_{m,N}$, and as a result $\eta_{SP,N}$, greatly increase, which leads to the conclusion that the N ionization rate is greatly enhanced at a higher V_d.

From the $\eta_{V,n}$ term, it is seen that $\eta_{V,N}$, perhaps surprisingly, is much higher (clearly outside the error bars) than η_{V,N_2}, and is even higher than η_V for xenon and argon, across all V_d. This indicates that, on average, N^+ and N_2^+ experience different ionization and acceleration regions, where the difference could occur either spatially or temporally. Gurciullo *et al.* measured acceleration voltages of ionic species of an air and xenon mixed propellant and also found that N^+ experienced a greater $V_{a,n}$ than N_2^+; however, the difference measured in that paper was not as apparent as is seen in Fig. 11. That may be due to the fact that the nitrogen propellant in this test was pure nitrogen as opposed to the air and xenon mixture used in Gurciullo *et al.* or the thruster is potentially running in a different operating mode than in Gurciullo *et al.*[36]

A large spatial variation between the N^+ and N_2^+ ionization and acceleration regions is not likely. Since N^+ is primarily created via a two-collision process, on average it would be produced further downstream than N_2^+. Plasma potential generally decreases monotonically away from the anode[13], so producing N^+ further downstream would cause N^+ to be born into a region with a lower plasma potential, resulting in $\eta_{V,N}$ being lower than η_{V,N_2}. This does not agree with the results shown in Fig. 11, so the N^+ and N_2^+ ionization regions must instead primarily differ temporally.

The traditional breathing mode instability for an atomic propellant HET consists of a rampant ionization phase causing fast neutral depletion and increase in ion number density followed by a neutral replenishment phase[54]. This instability appears as the discharge current exhibiting a sinusoidal behavior over time. For a HET operating on nitrogen, the nitrogen is injected as a neutral diatomic molecule. In the replenishment phase of the molecular breathing mode, the concentration of N_2 in the discharge channel will be much greater than the concentration of N. In the rampant ionization phase, N_2 will be quickly depleted into primarily N_2^+ and neutral N, since the dissociation and molecular ionization mechanisms are much more likely than a dissociative-ionization event. Throughout the rampant ionization phase, the concentration of neutral N in the discharge channel will quickly increase until N too begins ionizing. This will likely cause a secondary rampant ionization phase of primarily N^+ ions that is time-lagged from the N_2^+ ionization phase. This predicted characteristic behavior is shown in Fig. 12.
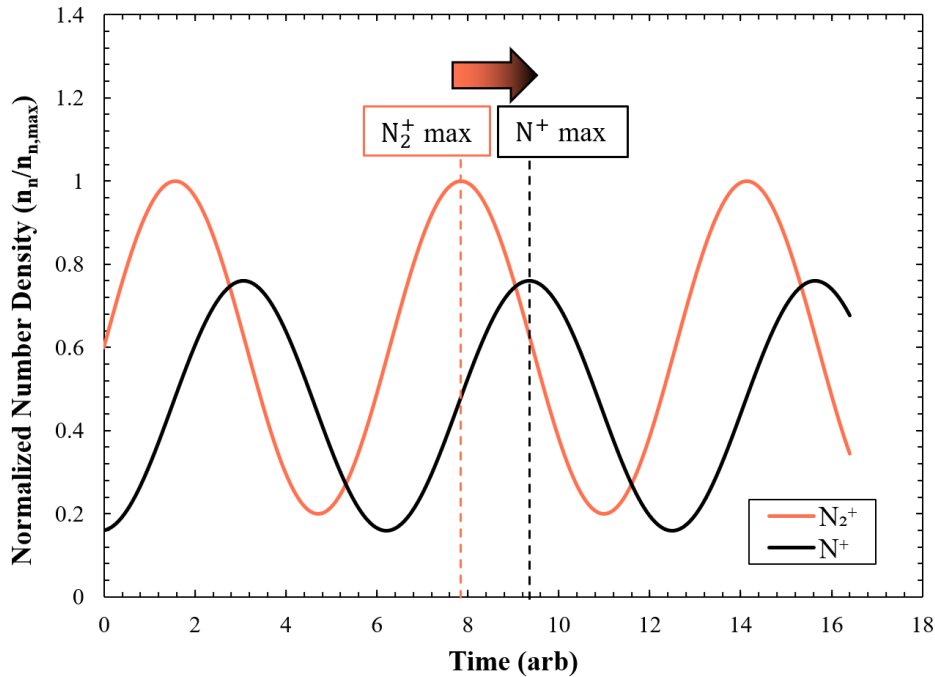

Figure 12. Predicted N_2^+ and N^+ number densities in a nitrogen-operated HET discharge channel as a function of time. Time units are arbitrary.

As seen in the above figure, the molecular breathing mode likely exhibits a complex behavior where N^+ production is time-lagged from N_2^+ production due to the time delay in the two-collisional ionization process for N^+. The plasma potential has also been shown to vary as a function of time in the HET discharge channel[55], and even if N^+ is born in a spatially similar location to N_2^+, its time-lagged behavior could allow it to be born in a region with a higher local

plasma potential. This behavior could explain why N^+ and N_2^+, on average, exhibit distinct acceleration voltages that likely originate from time-varying ionization and acceleration regions. This breathing mode theory can be tested experimentally in the future using a time-resolved RPA as outlined in Baird *et al.*[56]. If this theory holds, a time-resolved RPA can be used to generate an ion energy distribution function for each species.

Based on the results from this molecular efficiency approach, an optimized molecular HET should focus on either increasing the voltage utilization for the N_2^+ species and limit overall dissociation, or enhancing the dissociation rate and targeting an increased mass utilization of the N^+ species, potentially by operating at a higher V_d. The power split between the atomic and molecular pathways is likely largely determined by the strength of the dissociation mechanism in the dissociation region upstream of the ionization region. If this dissociation region can be controlled or modified by optimized HET design, power could potentially be influenced to travel down the preferred energy pathway for that thruster condition. The most efficient pathway to pursue is likely based on the primary power level in which the thruster will operate and the strength of the pathway-specific energy sinks at that power level.

V. Conclusion

This paper introduces a HET molecular energy flow model to visually represent the additional energy pathways and sinks present compared to atomic propellants. The molecular energy flow model influences the development of molecular mass utilization, voltage utilization, species fraction, and species parameter efficiency terms to characterize the relative efficiencies between producing N_2^+ and N^+ species and relate the impact of energy traveling down each of these pathways to overall thrust efficiency. Electron-impact kinetic mechanisms determine how the input power splits between the molecular energy pathways.

The authors apply the new molecular efficiency terms and energy flow model to experimental data from a 5-kW HET run on nitrogen, argon, and xenon to analyze the dominant kinetic mechanisms with nitrogen and how these mechanisms influence the resultant thrust efficiency. When analyzing species production as a function of discharge voltage, it was determined that a region must exist where dissociation is dominant over ionization, deemed the dissociation region. This region exists upstream of the ionization region and changes the neutral species concentrations that enter the ionization region, thus influencing the production rates of each species. When analyzing the molecular efficiencies, it was seen that a primary contributor to the low thrust efficiency seen with nitrogen is the poor mass utilization of the atomic nitrogen species. Another major, perhaps unexpected, finding was that the N^+ voltage utilization was much higher than the N_2^+ voltage utilization, which indicates that N_2^+ and N^+ on average experience different ionization and acceleration regions in a HET. The ionization regions between N_2^+ and N^+ most likely differ temporally, where the production of N^+ is time-lagged from N_2^+.

With a discharge voltage from 230-275 V, N_2^+ was seen to be the more efficient species to produce over N^+ due to its relatively higher mass utilization. For these test conditions, it was seen that stronger energy sinks existed on the atomic energy pathway compared to the molecular energy pathway. The dissociation kinetic mechanism directed energy toward the atomic pathway, which encountered these strong energy sinks, and degraded the overall nitrogen thrust efficiency. However, if thruster design or operating conditions are run to increase N mass utilization, the uniquely high acceleration potential experienced by N^+ could result in N^+ becoming the more efficient species to produce over N_2^+.

Acknowledgments

References

[1]Tisaev, M., Ferrato, E., Giannetti, V., Paissoni, C., Baresi, N., Lucca Fabris, A., and Andreussi, T., "Air-Breathing Electric Propulsion: Flight Envelope Identification and Development of Control for Long-Term Orbital Stability," *Acta Astronautica*, Vol. 191, Feb. 2022, pp. 374-393.
https://doi.org/10.1016/j.actaastro.2021.11.011.

[2]Crisp, N. H., Roberts, P. C. E., Livadiotti, S., Oiko, V. T. A., Edmondson, S., Haigh, S. J., Huyton, C., Sinpetru, L. A., Smith, K. L., Worrall, S. D., Becedas, J., Dominguez, R. M., Gonzalez, D., Hanessian, V., Molgaard, A., Nielsen, J., Bisgaard, M., Chan, Y. A., Fasoulas, S., Herdrich, G. H., Romano, F., Traub, C., Garcia-Alminana, D., Rodrigues-Donaire, S., Sureda, M., Kataria, D., Outlaw, R., Belkouchi, B., Conte, A., Perez, J. S., Villain, R., Heiberer, B., and Schwalber, A., "The Benefits of Very Low Earth Orbit for Earth Observation Missions," *Progress in Aerospace Sciences*, Vol. 117, Aug. 2020.
https://doi.org/10.1016/j.paerosci.2020.100619.

[3]Andreussi, T., Ferrato, E., Giannetti, V., Piragino, A., Cifali, G., Andrenucci, M., and Paissoni, C., "Development Status and Way Forward of SITAEL's Air-Breathing Electric Propulsion," AIAA Propulsion and Energy Forum, Indianapolis, IN, 2019.

[4]Dietz, P., Gartner, W., Koch, Q., Kohler, P. E., Teng, Y., Shreiner, P. R., Holste, K., and Klar, P. J., "Molecular Propellants for Ion Thrusters," *Plasma Sources Science and Technology*, Vol. 28, No. 8, 2019.
https://doi.org/10.1088/1361-6595/ab2c6c.

[5]Andreussi, T., Ferrato, E., and Giannetti, V., "A Review of Air-Breathing Electric Propulsion: From Mission Studies to Technology Verification," *Journal of Electric Propulsion*, Vol. 1, No. 31, 2022.
https://doi.org/10.1007/s44205-022-00024-9.

[6]Zheng, P., Wu, J., Zhang, Y., Wu, B., "A Comprehensive Review of Atmosphere-Breathing Electric Propulsion Systems," *International Journal of Aerospace Engineering*, Vol. 2020, Oct. 2020.
https://doi.org/10.1155/2020/8811847.

[7]Singh, L. A., and Walker, M. L. R., "A Review of Research in Low Earth Orbit Propellant Collection," *Progress in Aerospace Sciences*, Vol. 75, May 2015, pp. 15-25.
http://dx.doi.org/10.1016/j.paerosci.2015.03.001.

[8]Munro-O'Brien, T. and Ryan, C., "Performance of a Low Power Hall Effect Thruster with Several Gaseous Propellants," *Acta Astronautica*, Vol. 206, May 2023, pp. 257-273.
https://doi.org/10.1016/j.actaastro.2023.01.033.

[9]Marchioni, F. and Cappelli, M., "Extended Channel Hall Thruster for Air-Breathing Electric Propulsion," *Journal of Applied Physics*, Vol. 130, No. 5, 2021.
https://doi.org/10.1063/5.0048283.

[10]Ferrato, E., Giannetti, V., Califano, F., and Andreussi, T., "Atmospheric Propellant Fed Hall Thruster Discharges: 0D-hybrid Model and Experimental Results," *Plasma Sources Science and Technology*, Vol. 31, No. 7, 2022.
https://doi.org/10.1088/1361-6595/ac7904.

[11]Cifali, G., Misuri, T., Rossetti, P., Andrenucci, M., Valentian, D., Feili, D., and Lotz, B., "Experimental Characterization of HET and RIT with Atmospheric Propellants," 32nd International Electric Propulsion Conference, Wiesbaden, Germany, 2011.

[12]Hruby, V., Hohman, K., and Szabo, J., "Air Breathing Hall Effect Thruster Design Studies and Experiments," 37th International Electric Propulsion Conference, Cambridge, MA, 2022.

[13]Boeuf, J., "Tutorial: Physics and Modeling of Hall Thrusters," *Journal of Applied Physics,* Vol. 121, No. 1, 2017.
https://doi.org/10.1063/1.4972269.

[14]Su, L. L., and Jorns, B. A., "Performance Comparison of a 9-kW Magnetically Shielded Hall Thruster Operating on Xenon and Krypton," *Journal of Applied Physics*, Vol. 130, No. 16, 2021.
https://doi.org/10.1063/5.0066849.

[15]Hofer, R. and Gallimore, A. D., "High-Specific Impulse Hall Thrusters, Part 2: Efficiency Analysis," *Journal of Propulsion and Power*, Vol. 22, No. 4, 2006.
https://doi.org/10.2514/1.15954.

[16]Hofer, R. R., "Development and Characterization of High-Efficiency, High-Specific Impulse Xenon Hall Thrusters," Ph.D. Dissertation, Aerospace Engineering Department, University of Michigan, Ann Arbor, MI, 2004.

[17]Brown, D. L., Larson, C. W., Beal, B. E., and Gallimore, A., D., "Methodology and Historical Perspective of a Hall Thruster Efficiency Analysis," *Journal of Propulsion and Power*, Vol. 25, No. 6, 2009.
http://dx.doi.org/10.2514/1.38092.

[18]Brown, D. L., "Investigation of Low Discharge Voltage Hall Thruster Characteristics and Evaluation of Loss Mechanisms," Ph.D. Dissertation, Aerospace Engineering Department, University of Michigan, Ann Arbor, MI, 2009.

[19]Martinez, R. A., Dao, H., and Walker, M., "Power Deposition into the Discharge Channel of a Hall Effect Thruster," *Journal of Propulsion and Power*, Vol. 30, No. 1, 2014.
http://dx.doi.org/10.2514/1.B34897.

[20]Mazouffre, S., Dannenmayer, K., and Blank, C., "Impact of Discharge Voltage on Wall-Losses in a Hall Thruster," *Physics of Plasmas*, Vol. 18, No. 6, 2011.
https://doi.org/10.1063/1.3592251.

[21]Mikellides, I. G., Katz, I., Hofer, R. R., and Goebel, D. M., "Hall-Effect Thruster Simulations with 2-D Electron Transport and Hydrodynamic Ions," 31st International Electric Propulsion Conference, Ann Arbor, MI, 2009.

[22]Itikawa, Y., "Cross Sections for Electron Collisions with Nitrogen Molecules," *Journal of Physical and Chemical Reference Data*, Vol. 35, No. 1, 2006, pp. 31-53.
https://doi.org/10.1063/1.1937426.

[23]Cosby, P. C., "Electron-Impact Dissociation of Nitrogen," *The Journal of Chemical Physics*, Vol. 98, No. 12, 1993, pp. 9544-9553.
https://doi.org/10.1063/1.464385.

[24]Brook, E., Harrison, M. F. A., and Smith, A. C. H., "Measurements of the Electron Impact Ionisation Cross Sections of He, C, O, and N Atoms," *Journal of Physics B: Atomic and Molecular Physics*, Vol. 11, No. 17, 1978.
http://dx.doi.org/10.1088/0022-3700/11/17/021.

[25]Nagaraja, S., Yang, V., Adamovich, I., "Multi-Scale Modelling of Pulsed Nanosecond Dielectric Barrier Plasma Discharges in Plane-to-Plane Geometry," *Journal of Physics D: Applied Physics*, Vol. 46, No. 15, 2013.
http://dx.doi.org/10.1088/0022-3727/46/15/155205.

20

[26]Li, Z., Wu, E., Nie, L., Liu, D., and Lu X., "Magnetic Field Stabilized Atmospheric Pressure Plasma Nitrogen Fixation: Effect of Electric Field and Gas Temperature," *Physics of Plasmas*, Vol. 30, No. 8, 2023. https://doi.org/10.1063/5.0155713.

[27]Hleli, A., Riahi, R., Teulet, P., Cressault, Y., and Ghalila, H., "Calculation of Electron-Impact Excitation and Ionisation Cross Sections and Reaction Rate Coefficients for C, N, and O Atoms," 15th High-Tech Plasma Processes Conference, Toulouse, France, 2018. http://dx.doi.org/10.1088/1742-6596/1243/1/012014.

[28]Hayashi, M., "Bibliography of Electron and Photon Cross Sections with Atoms and Molecules Published in the 20th Century – Argon -," National Institute for Fusion Science NIFS-DATA-72, Jan. 2003.

[29]NIST Chemistry WebBook, National Institute of Standards and Technology SRD 69, retrieved 22 Feb. 2024. https://doi.org/10.18434/T4D303.

[30]Gaydon, A. G. and Penney W. G., "The Dissociation Energies of CO, N_2, NO, and CN", *Proceedings of the Royal Society of London A*, Vol. 183, No. 995, 1945, pp. 374-388. https://doi.org/10.1098/rspa.1945.0009.

[31]Gulczinski, F. S., "Examination of the Structure and Evolution of Ion Energy Properties of a 5kW Class Laboratory Hall Effect Thruster at Various Operational Conditions", Ph.D. Dissertation, Aerospace Engineering Department, University of Michigan, Ann Arbor, MI, 1999.

[32]Haas, J., "Low-Perturbation Interrogation of the Internal and Near-Field Plasma Structure of a Hall Thruster Using a High-Speed Probe Positioning System," Ph.D. Dissertation, Aerospace Engineering Department, University of Michigan, Ann Arbor, MI, 2001.

[33]Walker, M. L. R., "Effects of Facility Backpressure on the Performance Plume of a Hall Thruster", Ph.D. Dissertation, Aerospace Engineering Department, University of Michigan, Ann Arbor, MI, 2005.

[34]Polk, J., Haag, T., King, S., Walker, M., Blakely, J., and Ziemer, J., "Recommended Practice for Thrust Measurement in Electric Propulsion Testing," *Journal of Propulsion and Power*, Vol. 33, No. 3, 2017. https://doi.org/10.2514/1.B35564.

[35]Kim S. and Gallimore, A. D., "Plume Study of a 1.35-kW SPT-100 Using an ExB Probe," *Journal of Spacecraft and Rockets*, Vol. 39, No. 6, 2002. https://doi.org/10.2514/2.3897.

[36]Gurciullo, A., Fabris, A. L., and Cappelli, M. A., "Ion Plume Investigation of a Hall Effect Thruster Operating with Xe/N2 and Xe/air Mixtures," *Journal of Physics D: Applied Physics*, Vol. 52, No. 46, 2019. https://doi.org/10.1088/1361-6463/ab36c5.

[37]Huang, W. and Shastry, R., "Analysis of Wien Filter Spectra from Hall Thruster Plumes," *Review of Scientific Instruments*, Vol. 86, No. 7, 2015. http://dx.doi.org/10.1063/1.4923282.

[38]Lobbia, R. and Beal, B., "Recommended Practice for Use of Langmuir Probes in Electric Propulsion Testing," *Journal of Propulsion and Power,* Vol. 33, No. 3, 2017. https://doi.org/10.2514/1.B35531.

[39]Frieman, J. D., Brown, N. P., Liu, C. Y., Liu, T. M., Walker, M. L. R., Khayms, V., and King, D. Q., "Electrical Facility Effects on Faraday Probe Measurements," *Journal of Propulsion and Power: Technical Notes*, Vol. 34, No. 1, 2018. http://dx.doi.org/10.2514/1.B36467.

[40]Walker, M. L. R., Hofer, R. R., and Gallimore, A. D., "The Effects of Nude Faraday Probe Design and Vacuum Facility Backpressure on the Measured Ion Current Density Profile of Hall Thruster Plumes," 38th AIAA/ASME/SAE/ASEE Joint Propulsion Conference and Exhibit, Indianapolis, IN, 2002.

[41]Brown, D., Walker, M., Szabo, J., Huang, W., Foster, J., "Recommended Practice for Use of Faraday Probes in Electric Propulsion Testing," *Journal of Propulsion and Power,* Vol. 33, No. 3, 2017. https://doi.org/10.2514/1.B35696.

[42]Xu, K., "Ion Collimation and In-Channel Potential Shaping Using In-Channel Electrodes for Hall-Effect Thruster," Ph.D. Dissertation, Aerospace Engineering Department, Georgia Institute of Technology, Atlanta, GA, 2012.

[43]Piragino, A., Faraji, F., Reza, M., Ferrato, E., Piraino, A., and Andreussi, T., "Background Pressure Effects on the Performance of a 20 kW Magnetically Shielded Hall Thruster Operating in Various Configurations," *Aerospace*, Vol. 8, No. 3, 2021. https://doi.org/10.3390/aerospace8030069.

[44]Walker, M. L. R., Victor, A. L, Hofer, R. R., and Gallimore, A. D., "Effect of Backpressure on Ion Current Density Measurements in Hall Thruster Plumes," *Journal of Propulsion and Power*, Vol. 21, No. 3, 2005. https://doi.org/10.2514/1.7713.

[45]Randolph, T., Kim, V., Kaufman, H., Kozubsky, K., and Day, M., "Facility Effects on Stationary Plasma Thruster Testing," 23rd International Electric Propulsion Conference, Seattle, WA, 1993.

[46]Reid, B. M., "The Influence of Neutral Flow Rate in the Operation of Hall Thrusters," Ph.D. Dissertation, Aerospace Engineering Department, University of Michigan, Ann Arbor, MI, 2009.

[47]Taylor, B. N. and Kuyatt, C. E., "Guidelines for Evaluating and Expressing the Uncertainty of NIST Measurement Results," National Institute of Standards and Technology Technical Note 1297, 1994.

[48]Raitses, Y., Smirnov, A., Staack, D., and Fisch, N. J., "Measurements of Secondary Electron Emission Effects in the Hall Thruster Discharge," *Physics of Plasmas*, Vol. 13, No. 1, 2006.
http://dx.doi.org/10.1063/1.2162809.

[49]Wronski, Z., "Dissociation of Nitrogen in the Plasma-Cathode Interface of Glow Discharges," *Vacuum*, Vol. 78, No. 2, 2005, pp. 641-647.
https://doi.org/10.1016/j.vacuum.2005.01.113.

[50]Levaton, J., Klein, A. N., and Amorim, J., "Neutral and Excited Molecules and Atoms Densities in the Positive Column of Flowing N_2 DC Discharges," *Brazilian Journal of Physics,* Vol. 51, Oct. 2020, pp. 75-81.
https://doi.org/10.1007/s13538-020-00809-z.

[51]Kanazawa, S., Mizeraczyk, J., Nakatani, T., Kuno, A., Furuki, T., Tachibana, K., Ichiki, R., Kocik, M., "Implementation of a Single-Shot LIF Technique for 2-D Imaging of Metastable Nitrogen Molecules in a Discharge Afterglow at Sub-atmospheric Pressures," *Measurement*, Vol. 196, June 2022.
https://doi.org/10.1016/j.measurement.2022.111262.

[52]Cohen, L., and Hanson, R., "Emission and Laser-Induced Fluorescence Measurements in a Supersonic Jet of Plasma-Heated Nitrogen," *Journal of Physics D: Applied Physics*, Vol. 25, No. 3, 1992.
https://doi.org/10.1088/0022-3727/25/3/001.

[53]Haas, J. M., and Gallimore, A. D., "An Investigation of Internal Ion Number Density and Electron Temperature Profiles in a Laboratory-Model Hall Thruster," 36th AIAA/ASME/SAE/ASEE Joint Propulsion Conference and Exhibit, Las Vegas, NV, 2000.
https://doi.org/10.2514/6.2000-3422.

[54]Dale, E. T., "Investigation of the Hall Thruster Breathing Mode," Ph.D. Dissertation, Aerospace Engineering Department, University of Michigan, Ann Arbor, MI, 2020.

[55]Hagelaar, G. J. M., Bareilles, J., Garrigues, L., and Boeuf, J. P., "Role of Anomalous Electron Transport in a Stationary Plasma Thruster Simulation," *Journal of Applied Physics*, Vol. 93, No. 1, 2003, pp. 67-75.
https://doi.org/10.1063/1.1527218.

[56]Baird, M., McGee-Sinclair, R., Lemmer, K., and Huang, W., "Time-Resolved Ion Energy Measurements Using a Retarding Potential Analyzer," *Review of Scientific Instruments,* Vol. 92, No. 7, 2021.
https://doi.org/10.1063/5.0039621.